International Journal of Solids and Structures 241 (2022) 111454

Contents lists available at ScienceDirect

International Journal of Solids and Structures

journal homepage: www.elsevier.com/locate/ijsolstr

Morphometric description of strength and degradation in porous media

A. Guével [a,*], H. Rattez [b], E. Veveakis [a]

[a] Civil and Environmental Engineering Department, Duke University, Durham, NC 27708-0287, USA
[b] Institute of Mechanics, Materials and Civil Engineering (IMMC), Université Catholique de Louvain, B-1348 Louvain-la-Neuve, Belgium

ARTICLE INFO

Keywords:
Porous media
Morphometry
Strength
Resilience
Phase-field modeling
Degradation
Damage
Minkowski functionals

ABSTRACT

The influence of the microstructural geometry on the behavior of porous media is widely recognized, particularly in geomaterials, but also in biomaterials and engineered materials. Recent advances in imaging techniques, such as X-ray microcomputed tomography, and in modeling make it possible to capture the exact morphometry of the microstructure with high precision. However, most existing continuum theories only partially account for the morphometry. We propose here a unifying approach to link the strength of porous materials with the necessary and sufficient microstructural information, using Minkowski functionals, as per Hadwiger's theorem. A morphometric strength law is inferred from synthetic microstructures with a wide range of porosities and heterogeneities, through qualitative 2D phase-field simulations. Namely, damage is modeled at the microstructural level by tracking the solid-pore interfaces under mechanical loading. The strength is found to be best described by an exponential function of the morphometers, thus generalizing early works on metals and ceramics. We then show that the predictiveness of this relationship may extend to real porous media, including rocks, bones, and ceramics.

1. Introduction

Porous media represent a wide range of materials but also a tremendous challenge to be fully understood and harnessed. Among them, geomaterials, stemming from millions of years of transformations under harsh conditions, represent a particularly complex subclass, inasmuch as processes in these media are multiphysics and multiscales. Recent advances in geosciences found, however, that this complexity may boil down to the great heterogeneity and stochasticity of geomaterials' microstructures. For instance, pressure solution (Niemeijer et al., 2009; Croizé et al., 2013; van den Ende et al., 2019; Guével et al., 2020), strain localization (Vardoulakis and Sulem, 1995; Kawamoto et al., 2018), frictional instabilities (Rattez et al., 2018a,b), fault reactivation (Veveakis et al., 2014; Lesueur et al., 2020), and granular flow (Buscarnera and Einav, 2021) largely depend on the microstructural geometry, or *morphometry*. The same conclusion holds for engineered porous materials as well, such as ceramics (Salvini et al., 2018) and energetic materials (Chun et al., 2020). Biomaterials, forming a third subclass of porous media (Huyghe et al., 2002), are also increasingly studied in the light of their microstructures, in particular in bones mechanics (Augat and Schorlemmer, 2006; Wachter et al., 2002).

Therefore, modeling the microstructural dynamics is a crucial step towards better understanding the macroscopic behavior of porous media. In metallurgy, this has been achieved with phase-field modeling (Allen and Cahn, 1979; Provatas and Elder, 2010; Bhattacharyya et al., 2019), which tracks the grains interfaces through finite elements, and in geosciences, with discrete element modeling (O'Sullivan, 2011; Kawamoto et al., 2018), which tracks the grains as discrete elements, and recently also with phase-field modeling (Guével et al., 2020). That said, due to computational limitations, relying solely on microscopic simulations for large scales is unrealistic. On the other hand, the existing constitutive macroscopic laws rely heavily on destructive experimental calibration, which can be unfeasible because of the limited availability of materials or the impossibility to reproduce environmental conditions. For example, obtaining rocks from high depths can be prohibitively expensive or even impossible, and geological time scales are hardly reproducible in laboratory. As for biomaterials, such as bones, they are best studied in vivo (see Fragogeorgi et al. (2019) e.g.).

The correlation between the strength of materials and their microstructural geometry was first theorized, through the foundation of poromechanics, by Biot (1941), and for soils specifically, by Terzaghi (1943). This effort was intensified following the catastrophic failure of welded Allies ships through brittle fracture during the Second World War, with focus on metals and ceramics. The strength of brittle polycrystalline metals was quantitatively addressed by Orowan (1949), proposing what would ultimately become the Hall–Petch effect (Hall, 1951; Petch, 1953). The Hall–Petch relationship asserts that the yield stress, or similarly the flow stress, scales as the inverse square root of

* Corresponding author.
E-mail address: alexandre.guevel@duke.edu (A. Guével).

https://doi.org/10.1016/j.ijsolstr.2022.111454
Received 10 July 2021; Received in revised form 1 November 2021; Accepted 18 January 2022
Available online 3 February 2022

the mean grain size. However, Li et al. (2016) recently showed, upon critically reviewing a large amount of experimental data, that other types of laws, including inverse exponential, turn out as satisfying. Furthermore, Ryshkewitch (1953) experimentally found that the strength of porous brittle polycrystalline materials, such as ceramics, is an inverse exponential function of the porosity. This was confirmed more recently with porosity-controlled experiments and modeling by Liu et al. (2017). Building upon the previous results from non-porous and porous brittle materials, Knudsen (1959) inferred a multiplicative dependence of the strength on grain size and porosity (Eq. (7) therein), which was checked experimentally for ceramics at different temperatures. These efforts culminated to the advent of modern poromechanics (see Coussy (2004) and Dormieux et al. (2006)), reconciling continuum mechanics with Biot's theory, and relevant to a wide range of disciplines, including geo, bio and material sciences. However, the strength of porous media has mostly been studied with respect to porosity and grain size only. According to morphometry theory and in particular Hadwiger's theorem (see Armstrong et al. (2019) and Section 2.1), two more descriptors of the microstructure, which we refer to as *morphometers*, are needed to fully account for the morphometric effects. On these bases, we propose to investigate a morphometric strength law of the form:

$$\sigma_s = \sigma_s^* f(M_0/M_0^*, M_1/M_1^*, M_2/M_2^*, M_3/M_3^*), \tag{1}$$

where σ_s denotes the strength, as described in Section 3.1, the M_i (i = 0,…, 3) are the four required morphometers, the star quantities are reference values depending on the material and environmental conditions, and f is a multiplicative function of the M_i, following Knudsen (1959). In particular, M_0 denotes the porosity and M_2 the grain size. Our objective is to investigate the possible application of this law to porous materials in general, including geomaterials and biomaterials. Thereby, we subsume the microscopic mechanisms responsible for failure under the generic umbrella of damage. For geomaterials, this encompasses debonding, dissolution, cracks and breakage. Recent investigations in geosciences on the influence of the morphometry notably include the work of Zhang et al. (2016), Wetzel et al. (2021) and Buscarnera and Einav (2021). For biomaterials, in particular for bones, damage comprises dissolution, as in osteoporosis, and cracks, particularly in cortical bones (Augat and Schorlemmer, 2006). While the focus in biomechanics is mostly on the relationship between elastic moduli and morphometers, some results corroborate the conclusions inferred for the previous subclasses of porous materials, such as the exponential relationship between strength and porosity (see Wachter et al. (2002) and Appendix A). However, a mathematically-consistent law such as Eq. (1) has not been proposed yet, accounting for the necessary and sufficient microstructural information (see Section 2.1). In doing so, we advocate accounting for the simultaneous dependence of strength on multiple morphometers. This is particularly important for engineering materials since varying one morphometer will vary the others; for instance, decreasing the porosity to increase the strength may adversely increase the grain size (Knudsen, 1959). In addition, we intend to clarify which of the numerous morphometers used throughout the literature should be accounted for.

In order to numerically investigate the dependency of the strength of porous materials on their morphometers and specify Eq. (1), we control the variability of the morphometry by using synthetic microstructures (SMs). This also allows to run a sufficiently large, and hence statistically meaningful, ensemble of simulations and to account for the stochastic nature of real microstructures (Chun et al., 2020). Interest in synthesizing microstructures is intensifying in material sciences, owing to recent computational advances. In particular, machine learning enables to create highly realistic, tunable microstructures (Mosser et al., 2017; Chun et al., 2020). While the latter represents the state of the art, we have used, as a first step, a more straightforward and much less computationally-demanding approach (see Section 2.2).

In all, we aim here at bridging the gap between microscopic and macroscopic modeling, by calibrating macroscopic laws with morphometric parameters upscaled from simulations on synthetic microstructures, hinging, as much as possible, on non-destructive methods. We then check that the predictiveness of this relationship may extend to real porous media, by comparing with simulation results, through CT scans, and with existing experimental results. While complex multiphysics processes like pressure solution may still require explicit modeling of the microstructure (Guével et al., 2020), we suggest that as far as the influence of the microstructural geometry is concerned, it is possible to upscale only the essential morphometric information.

2. Methods

2.1. Upscaling of the microstructural information

The morphometers M_i in Eq. (1) are appropriately described by the Minkowski functionals of the domain formed by the grains Ω (Armstrong et al., 2019). Hadwiger's theorem guarantees that a microstructure is fully described by $d+1$ Minkowski functionals, where d is the space dimension, in the sense that any other descriptor that is additive, motion-invariant and conditionally continuous would be a linear combination of those functionals (see Hadwiger (1951) and also Klain (1995) for a short proof). Owing to the completeness of the set formed by the $d+1$ Minkowski functionals, we use these functionals as a mathematical basis for a necessary and sufficient accounting of the microstructural geometry. This result was originally derived in the context of integral geometry; thereby, an important underlying assumption is the convexity of the bodies upon which the Minkowski functionals are calculated. This is naturally the case, for instance, for granular media, which represent a large class of porous materials. However, non-convexity may occur locally when the grains have highly irregular shape; in that case, Hadwiger's result fails to hold, should a local convex approximation be impossible. In practice, customary tools for digital image analysis rely on an approximation of convexity. Namely, in watershed segmentation, utilized to discriminate the grains within a porous matrix, grains are usually locally approximated by spheres, similarly to the tools employed in this work (Gostick, 2017). This is based on the theory of "parallel bodies" approximating irregular shapes as a finite union of convex sets (Mecke and Arns, 2005). Particular attention should be paid to the accuracy of this approximation when a microstructure is dominated by non-convex shapes.

In 3D, the 4 needed Minkowski functionals are (Armstrong et al., 2019)

$$M_0(\Omega) = \int_\Omega \mathrm{d}V, \tag{2}$$

the total volume of the grains,

$$M_1(\Omega) = \int_{\partial\Omega} \mathrm{d}S, \tag{3}$$

their total surface area,

$$M_2(\Omega) = \int_{\partial\Omega} \left(1/r_1 + 1/r_2\right) \mathrm{d}S, \tag{4}$$

their total mean curvature, where r_1 and r_2 denote the principal radii of curvature of the surface element $\mathrm{d}S$, and

$$M_3(\Omega) = \int_{\partial\Omega} \left(1/r_1 r_2\right) \mathrm{d}S = 4\pi\chi(\Omega), \tag{5}$$

their total Gaussian curvature, directly related to the Euler characteristic χ by the Gauss–Bonnet theorem (Armstrong et al., 2019). In turn, the Euler characteristic is directly related to the grains, or pores, connectivity (Vogel, 2002). In practice, we will use the porosity n as a measure of M_0 and the mean grain size g for M_2, which approximates the inverse of the average mean curvature. The latter approximation is in line with the typical algorithms that calculate the mean curvature

of the grains obtained from watershed segmentation by approximating them by equivalent spheres, as detailed in the next section. For simplicity, we keep the notations M_0 and M_2 for those quantities. In this contribution, we will restrict our results to $d = 2$ as a first step, and therefore use only 3 morphometers to constrain the strength law Eq. (1).

2.2. Synthetic microstructures

To find the function $f(M_i)$ in Eq. (1), we run a large amount of simulations on SMs, which are generated using the Python open-source package `PoreSpy`[1] (Gostick et al., 2019). The starting point is a random noise (see Fig. 1a), that is, a 2D array $R[i,j]$ ($i = 0,\dots,N-1$, $j = 0,\dots,N-1$), of dimension N, of random values between 0 and 1. It is then convoluted with a Gaussian filter (see Fig. 1b)

$$G[i,j] = e^{-\frac{i^2+j^2}{2s^2}}, \tag{6}$$

which standard deviation $s = \frac{N}{40h}$, or blurriness, is inversely proportional to a heterogeneity parameter h, and where 40 is a scaling factor; the heterogeneity of the output is then independent from the image size. The filtered output $F[i,j]$ is thus calculated as follows (see Gonzalez and Woods (2008) e.g.):

$$F[i,j] = R[i,j] * G[i,j] = \sum_{u=0}^{N-1}\sum_{v=0}^{N-1} R[u,v]G[i-u,j-v], \tag{7}$$

where $*$ denotes the convolution operator. Finally, after uniformizing the blurred noise $F[i,j]$ between 0 and 1, the array is binarized into $B[i,j]$ (see Fig. 1c) by using the porosity n as the threshold, yielding the final SM. The two input parameters controlling the generation of the SMs are thus the heterogeneity h and the porosity n. We will see that h controls the narrowness and skewness of the morphometers distributions. To restrict the study to realistic microstructures, n is varied from 0.15 to 0.4 and h from 2 to 5, creating an ensemble of 42 SMs (see Appendix B). This ensemble forms the training batch, from which the dependence of the strength on the morphometry will be inferred. Throughout this work, the dimensions of the synthetic SMs are restricted to 200×200 pixels, as a compromise between sufficiently realistic microstructures and reasonable mesh sizes, which increase with this resolution. It is then possible to obtain the distributions of the morphometers M_0, M_1, M_2, i.e. of the pore size, perimeter and grain size, respectively, starting with the marker-based watershed segmentation algorithm introduced by Gostick (2017). The values of the filter size and of the Gaussian blur therein are carefully chosen to maximize the number of segmented regions (grains or pores). Thereby, we minimize the error made in the aforementioned convex approximation, which enforces Hadwiger's theorem. In particular, since the optimal values for those parameters vary with the grain/pore size, they are expected to vary with h. Namely, we found that the filter size varies from 2 to 9 pixels for our range of SMs, whereas the blur varies from 0.2 to 0.8. Upon segmenting the pores, their sizes are obtained by determining the equivalent disks for every pores. Upon segmenting the grains, their perimeter is obtained via an edge-finding algorithm optimized for fast computing introduced by Benkrid et al. (2000). The grain sizes are obtained similarly to the pore sizes. The last morphometer M_3, the Euler characteristic, is not concerned by distributions since it is a topological quantity. While the distributions of M_0 and M_1 are useful when comparing the SMs with real microstructures (see Section 3.4), only the grain size distribution is calculated for every SMs, in order to determine the mean grain size M_2. The latter is taken as the mean of the lognormal fit of the grain size distribution, as explained in Section 3.4. M_0 and M_1 are directly obtained from calculating the porosity, i.e. the ratio of the black pixels over the total number of pixels, and the total perimeter, respectively. Finally, the Euler characteristic M_3 is calculated from an integral geometry formula in discretized space. In the current 2D restriction, M_3 is simply the number of objects minus the number of holes. We refer to the documentation of `PoreSpy` and `skimage` available online for further details (see Appendix C).

[1] http://porespy.org.

2.3. Damage phase-field modeling of the microstructure

The evolution of the microstructure is modeled via a phase field φ differentiating the pores from the grains, as introduced in Guével et al. (2020), and describing the damage of the grains. As such, the phase field measures the morphometric variations, and thus controls the evolution of the morphometers (see Section 3.6). For all simulations, we use the open-source multiphysics finite-element platform `MOOSE` (Permann et al., 2020). Following Guével et al. (2020), the phase-field equation stems from the coupling of the microscale mechanics (at the grains scale) and the macroscale mechanics (mixture of grains and pores). The former is governed by the micro-momentum balance (Fried and Gurtin, 1993; Gurtin, 1996) and the latter by the usual macro-momentum balance, as given, respectively, by

$$\begin{cases} \nabla\cdot\boldsymbol{\xi} + \pi = 0, \\ \nabla\cdot\boldsymbol{\sigma} = 0, \end{cases} \tag{8}$$

where $\nabla\cdot$ denotes the divergence, π is the microforce (scalar), energy-conjugate of φ, $\boldsymbol{\xi}$ is the microstress (vector), energy-conjugate of $\nabla\varphi$, and $\boldsymbol{\sigma}$ is the Cauchy stress tensor. The two momentum balances are coupled via the *generalized relaxation equation* (Guével et al., 2020), equivalent to the second law of thermodynamics as described by the dissipation inequality

$$-\dot{\psi} - \pi\dot{\varphi} + \boldsymbol{\xi}\cdot\nabla\dot{\varphi} - \boldsymbol{\sigma} : \dot{\boldsymbol{\epsilon}} \le 0, \tag{9}$$

where ψ is the free energy, the superposed dot denotes the time derivative, the dot operator the scalar product, and the double-dot operator the tensorial product. The free energy is described in its usual Landau form (Landau, 1937) through

$$\psi(\varphi,\nabla\varphi,\boldsymbol{\epsilon}) = Gg(\varphi) + (1-h(\phi))\frac{1}{2}\boldsymbol{\epsilon}\cdot\boldsymbol{C}_p\boldsymbol{\epsilon} + h(\varphi)\frac{1}{2}\boldsymbol{\epsilon}\cdot\boldsymbol{C}_g\boldsymbol{\epsilon} + \frac{\kappa}{2}|\nabla\phi|^2, \tag{10}$$

where G is the height of the double-well potential, κ the interfacial energy coefficient, the polynomials $g(\varphi) = \varphi^2(1-\varphi)^2$ and $h(\varphi) = \varphi^2(3-2\varphi)$ correspond to a double-well potential and an interpolation function, and $\boldsymbol{C}_g$ and $\boldsymbol{C}_p$ denote the elastic tensor of the grains and the pores, respectively. The micro-mechanical properties are homogenized through the Voigt–Taylor homogenization scheme (see Ammar et al. (2009) and Aagesen et al. (2017)), which consists in interpolating the partial stresses of the grains and pores phases while assuming homogeneous strains, thus recovering a familiar poromechanics formulation. Thereby, $\boldsymbol{C}(\varphi) = (1-h(\varphi))\boldsymbol{C}_p + h(\varphi)\boldsymbol{C}_g$ is the elastic tensor of the mixture, and the Cauchy stress tensor reads $\boldsymbol{\sigma} = \boldsymbol{C}(\varphi)\boldsymbol{\epsilon}$. We note that the choice of the homogenization scheme may affect the outcome of quantitative simulations (Aagesen et al., 2017), but we focus here on qualitative results only.

From a thermodynamic perspective, the state variables are φ, describing the normal variations of the grains interface, $\nabla\varphi$, describing the tangential variations of the grains interface, and $\boldsymbol{\epsilon}$ the macroscopic (elastic) strain tensor. For simplicity, we consider $\nabla\varphi$ and $\boldsymbol{\epsilon}$ to be non-dissipative, thus neglecting viscous effects; the viscous effect associated with the phase field would delay phase changes as shown in Guével et al. (2020). Furthermore, differently from Guével et al. (2020), we neglect the gyroscopic chemical coupling that would allow grain healing; namely, the relaxation potential, which completes the energy potential ψ and relates the rates of the state variables to the thermodynamic forces, is taken diagonal. Thereupon, the three relaxation equations,

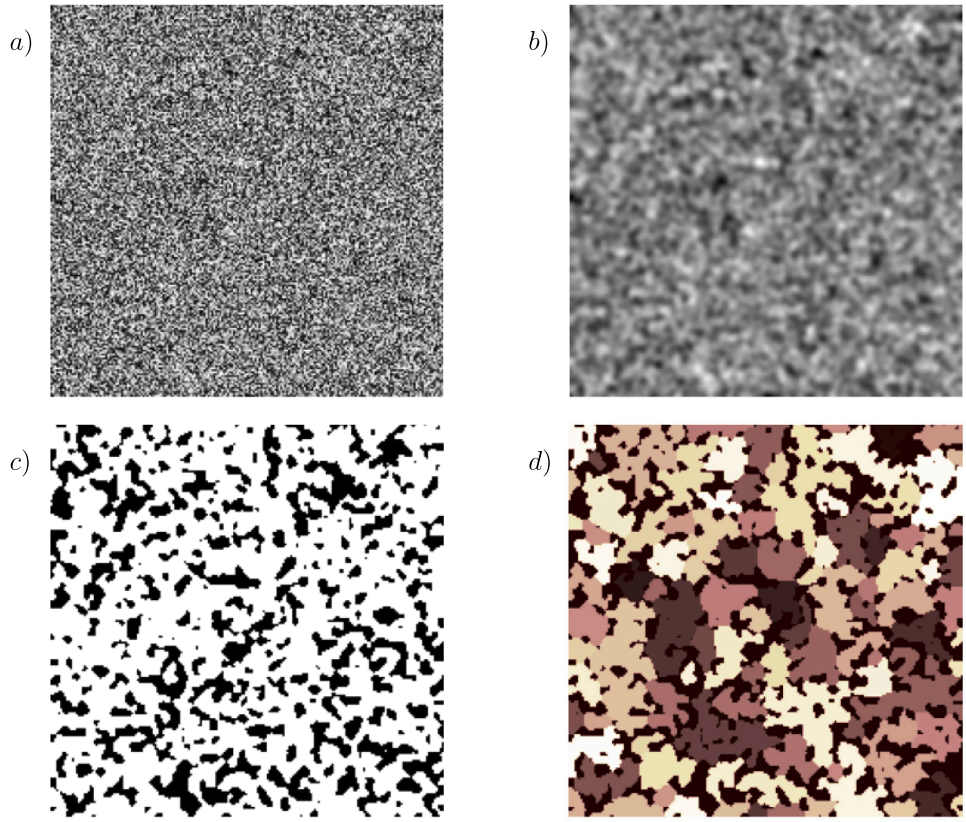

Fig. 1. a) Random noise $R[x, y]$, i.e. array of random values between 0 and 1. b) Gaussian filter $F[x, y]$ applied onto the random noise, with a standard deviation of 1.76, or equivalently, $h = 3$. c) Resulting binarized SM $B[x, y]$ upon applying the threshold $n = 0.3$. d) SM segmented into 110 grains via watershed algorithm.

which constrain the model's equations to satisfy the second law Eq. (9), read

$$\begin{cases} \tau\dot{\varphi} = -\pi - \frac{\partial\psi}{\partial\varphi}, \\ 0 = \boldsymbol{\xi} - \frac{\partial\psi}{\partial\nabla\varphi}, \\ 0 = \boldsymbol{\sigma} - \frac{\partial\psi}{\partial\boldsymbol{\epsilon}}, \end{cases} \tag{11}$$

where τ is the relaxation time associated with φ. Combining the momentum balances (8) and the relaxation Eqs. (11) yields the following Allen–Cahn equation, coupled with elastic mechanics:

$$\begin{cases} \tau\dot{\varphi} = \kappa \,\triangle\, \varphi - Gg'(\varphi) - \lambda(\boldsymbol{\epsilon})h'(\varphi), \\ \nabla \cdot \boldsymbol{C}(\varphi)\boldsymbol{\epsilon} = 0, \end{cases} \tag{12}$$

where $\lambda(\boldsymbol{\epsilon}) = 1/2(\boldsymbol{C}_g - \boldsymbol{C}_p)\boldsymbol{\epsilon} \cdot \boldsymbol{\epsilon}$ denotes the difference of elastic energy between the grains and pores phases.

The encompassing concept behind modeling damage with a phase field is the tilting of the double-well potential $Gg(\varphi)$, upon input of mechanical energy, beyond the saddle–node bifurcation point (Guével et al., 2020), that is, beyond the activation energy of the damage process considered. In the present study, we leave our model agnostic of the specific nature of damage, upon assuming that only the level of activation energy will differ from a type of damage to another. Thereupon, in the present description, damage is not specified but may include debonding, dissolution and microcracking, the choice of which would depend on the amount of mechanical energy input and the time scale. For instance, over long time scales, such as in geological settings, damage may correspond to dissolution, as detailed in Guével et al. (2020) studying pressure solution with a model similar to (12). This model could also be applied when damage corresponds to microcracking. Indeed, (12) is similar to the model used for modeling fractures at the continuum scale (see Kuhn and Müller (2010) e.g.). The fundamental difference is that our model is applied directly at the grains scale, whereas phase-field damage models have so far been applied to the continuum scale. Hence, instead of the usual differentiation between the intact and the damaged phases, our model differentiates between the grains and the pores phases, where the growth of the pores phase at the expense of the grains phase embodies the microstructural damage. We distinguish the latter from its upscaled manifestation at the continuum scale, which we call the *degradation* (see Section 3.6). In particular, while the damaged phase in the macroscopic theory is not energetic, here, the pores phase is associated with an elastic energy (albeit not allowing shearing), yielding a mixture of elastic energies, as described above. Therefore, the only differences in the form of our phase-field equation with the continuum damage phase-field modeling are the presence of an elastic energy for the phase $\varphi = 0$ and the degrees of the polynomials representing the potential $g(\varphi)$ and the interpolation function $h(\varphi)$. Similar models in the literature include also the one used for grain growth in (non-porous) metals under mechanical loading (see Tonks and Millett (2011) e.g.), where each grain of a polycrystal is represented by an order parameter. Unlike for metals, the pores phase in porous media such as geomaterials plays a crucial role, so that it is given an independent role in our model. The main difference between modeling porous media and metals is thus that we discriminate the pores from the skeleton, without differentiating, as a first step, the different grains, inasmuch as they are not necessarily distinguishable within the skeleton, depending on the materials; for instance, as discussed in the following, unlike a sandstone, a cortical bone can hardly be decomposed into grains. In practice, this translates into dropping the grain-to-grain interfacial energy term present in the polycrystals phase-field model. In all, modeling the microstructural damage of porous media is performed here as a combination of the concepts used in continuum damage and polycrystals phase-field modeling. In practice, since we focus mostly on tensile loadings, one may expect that damage

would occur through debonding or microcracking, both for the geo and biomaterials considered here.

Upon choosing a characteristic length l_0, a characteristic time $t_0 = \tau/G$ and a characteristic specific energy $G = 1\,\text{GPa}$, we write (12) in dimensionless form as follows:

$$\begin{cases} \dot{\varphi} = \hat{\kappa} \triangle \varphi - g'(\varphi) - \hat{\lambda}(\epsilon) h'(\varphi), \\ \nabla \cdot \hat{\boldsymbol{C}}(\varphi)\boldsymbol{\epsilon} = 0, \end{cases} \tag{13}$$

where $\hat{\kappa} = \kappa/Gl_0^2$ is the (dimensionless) interfacial group, $\hat{\lambda} = \lambda/G$ is the activation energy group and $\hat{\boldsymbol{C}} = \boldsymbol{C}/G$. The dimensionless derivatives are noted similarly and the hat notation for dimensionless quantities is dropped in the following. The evolution of the damage via φ is fully determined by λ, upon fixing κ to an appropriately small value (see Section 3.3). We also restrict our attention for simplicity to 2D problems, so that the elastic energy λ is fully determined by the two Lamé parameters. As explained in Guével et al. (2020), the grains are considered as solids of very low porosity, and the pores as shear-free solids that are much more deformable. Namely, for geomaterials, we choose the first and second Lamé parameters of the grains both to be that of granite 30 GPa, and for the pores 1 GPa and 0, respectively. Further major assumptions include small strains and that the assembly of grains considered is representative of the material. To focus on the effect of the microstructure on the strength, we will first perform simulations in tension with fixed lateral boundaries. Then, to determine the effect of the confinement, we will perform axisymmetric biaxial loadings. As noted by Knudsen (1959), experimental data from the literature suggest that the nature of the morphometric function f in Eq. (1) should be valid for different strength tests, whether in compression, tension, or bending (see Section 4.2). Throughout this work, the invariant measure of stress used in output is the von Mises stress, which is directly related to the second invariant of the deviatoric stress. The associated strain is the vertical displacement of the top boundary divided by the initial length of the square domain.

3. Model's performance

3.1. Measure of the strength

In solid mechanics, the word "strength" has a broad meaning. Most often, it corresponds to the maximum value that the stress can attain (peak stress). Alternative measures of strength include the yield stress, or even the value of stress at a given value of strain when the material is undergoing prolonged hardening (Sari et al., 2020; Fischer and Paterson, 1989). Since the latter is the case in the present study, the strength is defined throughout this work as a value of the vertical stress for a certain value of a post-yield deformation ϵ_s attributed to a given material. The latter is determined for the SMs a posteriori, after obtaining the stress–strain output for all the training batch, as the minimum yield strain. Namely, as shown in Fig. 2 for 16 of the 42 SMs, we find that $\epsilon_s = 11.5\%$ is the minimum strain required for all the SMs to enter yielding, that is, so that the stress–strain response is non-linear. The ϵ_s-strength, noted σ_s, also called flow stress (Fischer and Paterson, 1989), is the value of the aforementioned stress invariant corresponding to this value of ϵ_s. It will be determined similarly for the real microstructures.

3.2. Mesh convergence

Before obtaining any meaningful results, it is important to study the mesh convergence. The initial conditions of the simulations are indeed determined by digitizing the input image, with respect to the chosen mesh dimensions. In particular, smaller microstructural dimensions require a finer mesh. Therefore, we expect to use finer meshes for SMs of smaller grain sizes. We refer to Appendix B for the summary of the grain sizes of our training batch. To assess the mesh convergence, we compare the values of σ_s for the different SMs, to find that, indeed, the

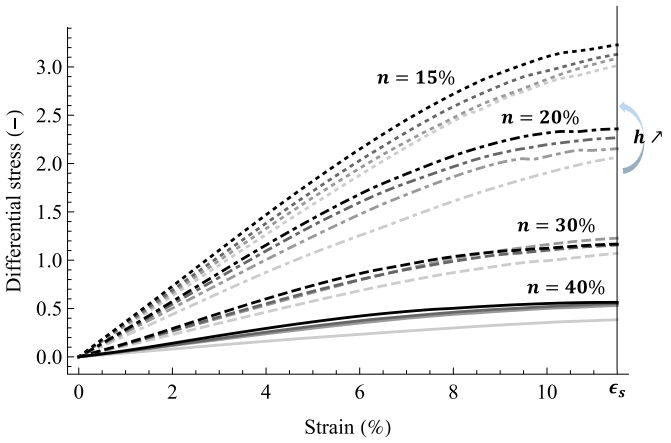

Fig. 2. Stress–strain responses for 16 of the 42 SMs ($n \in \{0.15, 0.20, 0.30, 0.40\}$, $h \in \{2, 3, 4, 5\}$) until $\epsilon_s = 11.5\%$, showing that all the SMs reach post-yield for this value. Changes from dotted to full lines correspond to an increase in porosity n, and increases in gray intensity to an increase in heterogeneity h. The rest of the SMs corroborates this assertion but are not shown here for visibility purposes.

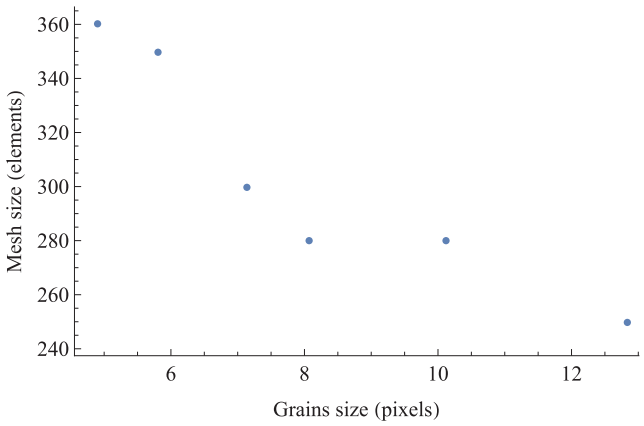

Fig. 3. Evolution of the minimum mesh size (number of elements per side of the domain) required for mesh convergence with respect to the grain size.

Table 1
Number of elements used for the meshes in our simulations for different mean grain sizes.

Mean grain size (px)	Mesh size (elts)
4–6	360 × 360
6–7	350 × 350
7–8	300 × 300
8–13	280 × 280

mesh dimensions increase with the grain size (see Fig. 3). We then pick the minimum mesh size required for mesh convergence within a 2% error. In practice, using Fig. 3, we use the mesh sizes shown in Table 1. Note that the grain sizes are measured in pixels where $1px = l_0/N$, l_0 is the characteristic length of the problem taken as the image size and N the image dimension. When l_0 is determined in the case of real microstructures, the length measurements will be given in mm (or μm) in the following.

3.3. Influence of the interfacial coefficient κ

While the activation energy $\lambda(\epsilon)$, coupled with the mechanical energy, is the main drive for the phase change, the interfacial coefficient κ quantifies its diffusive character. When $\kappa \gg \lambda$, that is, when the activation energy is negligible compared to the interfacial energy, the process

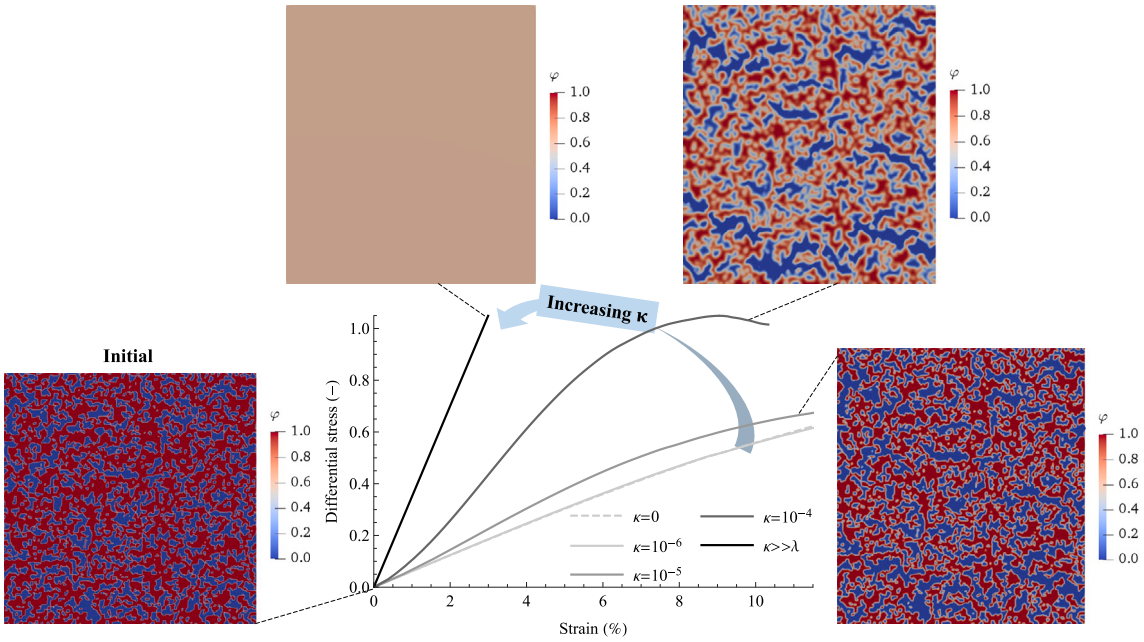

Fig. 4. Mechanical response of the SM ($n = 0.4, h = 5$) for different values of κ, including the limit cases $\kappa = 0$ (sharp interface) and $\kappa \gg \lambda$ (pure diffusion). Note the spurious diffusion in the case $\kappa = 10^{-4}$, leading to the closure of the smallest pores, as opposed to the case $\kappa = 10^{-5}$.

is purely diffusive, and therefore nonphysical in the current context. Conversely, when $\kappa \to 0$, the process falls back on the corresponding sharp interface problem, thereby losing the regularization provided by the diffuse interfaces, characteristic of phase-field modeling. We thus choose the value of κ not too large to avoid spurious interfacial diffusion, but not too low to keep diffuse interfaces. The former would typically induce the closure of the smallest pores, independently from the mechanical loading. To do so, we perform simulations for different values of κ, while the microstructure and the other parameters are fixed. To be conservative, we choose the SM with the smallest mean grain size in our training batch, namely for $(n = 0.4, h = 5)$. Indeed, spurious diffusion will occur first for the smallest microstructural length scales. Note that more elaborated techniques exist to circumvent spurious kinetic effects (see Tourret et al. (2021) and references therein). We choose $\kappa = 10^{-5}$ since for $\kappa \geq 10^{-4}$, spurious diffusion occurs, whereas for $\kappa \leq 10^{-6}$, the results are similar to the case where $\kappa = 0$ (see Fig. 4). Specifically, it can be seen that for $\kappa \geq 10^{-4}$ the smallest pores close under diffusion of the grains phase, as opposed to the case where $\kappa \leq 10^{-5}$. The limit case $\kappa \gg \lambda$ of pure diffusion is also shown in Fig. 4, where, after only one timestep, the microstructure mixes into a homogeneous phase where $\varphi \approx 0.6$. Thereupon, the mechanical response is that of a homogeneous elastic solid, which homogenized elastic modulus can be estimated around 3.5.

3.4. Resemblance of the SMs with real microstructures

Before drawing realistic results from the SMs, let us also check how representative they are of real microstructures. We find that the SMs resemble real microstructures through the distributions of the three first morphometers. We find that the grain size distributions of the SMs are skewed towards smaller grains (i.e. right-tailed), as expected from thresholding the initial symmetric Gaussian noise. The heterogeneity h controls their skewness (i.e. deviation from a normal distribution) and narrowness (see Fig. 5). The distributions of SMs with larger heterogeneity h are less skewed but narrower. More precisely, the SMs exhibit lognormal distributions (see Fig. 6), similarly to a large variety of porous media. This type of distribution can be found in geomaterials (see Hwang and Powers, 2003; Marks and Einav, 2015 and references therein), as well as engineered porous materials (see Liu et al. (2017) e.g.). For direct comparison, we consider a Mt Simon sandstone, presented in Kohanpur et al. (2020), and digitalized on digitalrocksportal.org, of average porosity 27.1%. Each sides of the CT scans have a resolution of 1200 pixels measuring each 2.8 µm. To imitate a given slice of porosity 27.4% (Fig. 6a), we generate a SM (Fig. 6e) of same porosity and resolution, and of heterogeneity h determined to match the mean grain size. The distributions of the three first morphometers for the real and synthetic microstructure are compared in Fig. 6 and Table 2, and checked to be both well fitted by lognormal distributions.

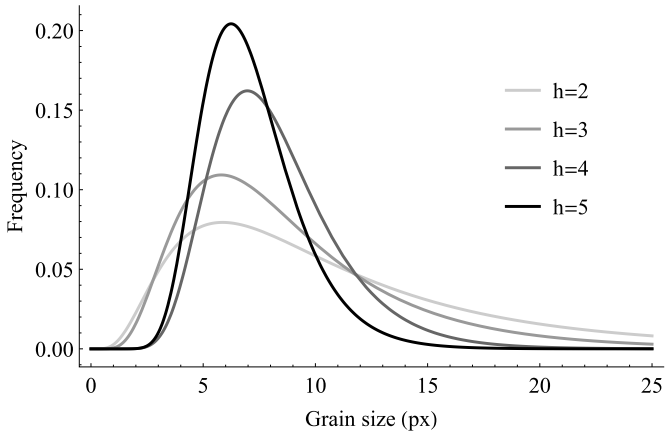

Fig. 5. Evolution of the grain size distribution with the heterogeneity h for a fixed porosity $n = 0.2$ for a 200×200 pixels resolution, showing that higher values of h lead to less skewed but narrower distributions. Indeed, the skewness values, calculated as Pearson's moment coefficient of skewness, are found here to be 2.75 for $h = 2$, 1.96 for $h = 3$, 1.07 for $h = 4$, 0.95 for $h = 5$.

3.5. Determinism of the SMs

Since the generation of the SMs starts from a random noise, it is not a priori deterministic. Indeed, varying the random seeds for a given set of input parameters n and h yields different microstructures. To

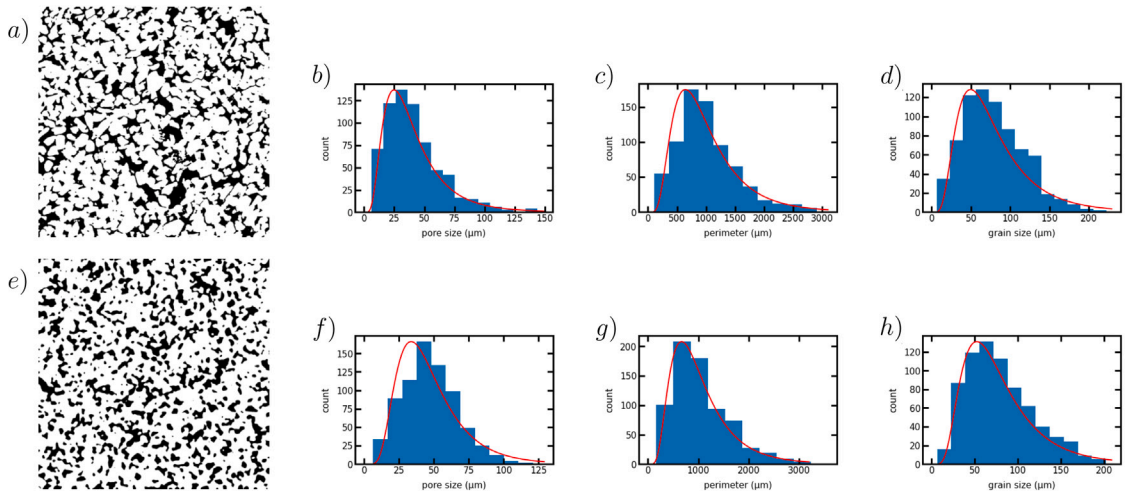

Fig. 6. a) CT scan of Mt Simon sandstone segmented into 733 grains, of porosity $M_0 = 27.4\%$ (mean pore size 41.51 μm), total perimeter $M_1 = 190.11$ mm (mean perimeter 1.02 mm), mean grain size $M_2 = 79.80$ μm and Euler number $M_3 = -351$, along with the associated lognormally-fitted distributions in b), c), d) respectively. e) SM generated for $n = 27.4\%$ and $h = 3.9$ with resolution 1200 × 1200 pixels, matching the sandstone microstructure, segmented into 717 grains, of porosity $M_0 = 27.4\%$ (mean pore size 47.49 μm), total perimeter $M_1 = 167.17$ mm (mean perimeter 1.06 mm), mean grain size $M_2 = 79.26$ μm and Euler number $M_3 = -202$, along with the associated distributions in f), g), h) respectively.

Table 2
Comparison of the morphometers of the Mt Simon sandstone with the synthetic analogue, along with the mean values of their lognormal distributions.

	Sandstone	Synthetic	Error (%)
Porosity M_0 (%)	27.4	27.4	0
Perimeter M_1 (mm)	190	167	12
Mean grain size M_2 (μm)	79.8	79.3	0.68
Mean pore size (μm)	41.5	47.5	14
Mean perimeter (mm)	1.02	1.06	3.9

quantify the influence of this discrepancy on the mechanical response, we compare the numerical results for $n = 0.3$, $h = 3$ as an example, with 10 different seeds (see Appendix D). Namely, we calculate the set of strengths σ_s (for $\epsilon_s = 11.5\%$) for the different seeds. We find that the standard deviation of this set divided by its mean is around 4%, which we consider as an approximate measure of the potential error in the following predictive fitting.

3.6. Morphometers evolution

Numerical results are shown in Fig. 7 for the SM $n = 0.2$ and $h = 5$, from the initial SM input, which digitization provides the initial conditions for the phase field φ, to the (post-yield) state where the strength is reached. The associated distributions of the volumetric strain and of the phase-field rate illustrate the causality between mechanical loading and damage. Upon tensile loading, the pores open up, leading to damage events responsible for failure, namely the coalescence of neighboring pores, well known possible microstructural manifestation of strain hardening (Pardoen and Hutchinson, 2000). This can represent debonding or microcracks. In this particular example, the main damage event (maximum of $|\dot{\varphi}|$) responsible for failure occurs in the center (see black oval in Fig. 7). As a macroscopic descriptor of the microscopic damage, we define the relative degradation D_r, similarly to breakage mechanics (Einav, 2007), so that $D_r = 0$ corresponds to an undamaged material and $D_r = 100\%$ to a final state of damage. The latter is arbitrarily defined as the state where the strength is reached (see Section 3.1). Thus, D_r is a relative measure of degradation, as it depends on the initial and final state considered, and is calculated as the following upscaling function:

$$D_r = \frac{\int_{\bar{\Omega}} \varphi(\epsilon)\mathrm{d}\epsilon - \int_{\bar{\Omega}} \varphi(\epsilon_0)\mathrm{d}\epsilon}{\int_{\bar{\Omega}} \varphi(\epsilon_s)\mathrm{d}\epsilon - \int_{\bar{\Omega}} \varphi(\epsilon_0)\mathrm{d}\epsilon}, \tag{14}$$

where $\bar{\Omega}$ denotes the total spatial domain, $\epsilon_0 = 0$, ϵ_s is the strain when σ_s is reached, so that $\int_{\bar{\Omega}} \varphi(\epsilon)\mathrm{d}\epsilon$ computes the domain's portion occupied by the grains, since $\varphi = 1$ represents the grains and $\varphi = 0$ the pores. The evolution of the relative degradation of the SM of Fig. 7 with respect to the strain is shown in Fig. 8, along with the corresponding stress–strain curve and the evolution of the 4 morphometers; although only 3 morphometers are required in 2D to fully constrain the strength law, we find it informative to include all of them here. As expected, the tensile loading opens up the pores, which increases the porosity $n = M_0$. Moreover, as the neighboring pores merge with each other towards failure (see Fig. 7), the number of pores decreases (by around 9%) and therefore, the Euler characteristic $\chi = M_3$ decreases in absolute value. As a consequence, the total perimeter M_1 decreases and the mean grain size M_2 increases, although both by less than 5%, as opposed to M_0 and M_3 varying by around 20%. The observed morphometers evolution is consistent with the evolution of strength found later in Section 4.1 with respect to the initial morphometers values. Indeed, the material weakens upon loading, and therefore can be seen as a strong material initially and as a weaker one at the end of the loading. Consistently, we find that the strength decreases with the porosity M_0 and the mean grain size M_2, but increases with the total perimeter M_1 and the absolute value of the Euler characteristic M_3.

4. Results

4.1. Scaling of the strength with the morphometers in SMs

We now gather the results of all the simulations on the 42 SMs (see Appendix B), to find the best-fit function $f(M_i)$ relating the strength to the morphometers, via the least squares method. The latter is adequate since no outliers are expected in the present synthetic numerical data set (as opposed to a set of experimental data). In the present 2D case, we only need 3 morphometers, chosen as M_0, M_1 and M_2 for instance. Following our initial assumption of a multiplicative dependence of the strength on the morphometers, as a generalization of Knudsen's theory (Knudsen, 1959), we find that the best fit is exponential, with an adjusted r^2 coefficient of 0.9995 and an average error of 2.67%, as compared with other potential candidates (see Table 3). In the present 2D case, the strength law Eq. (1) thus reads

$$\sigma_s = \sigma_s^* e^{-\frac{M_0 - M_0^*}{M_0^*} + \frac{M_1 - M_1^*}{M_1^*} - \frac{M_2 - M_2^*}{M_2^*}}. \tag{15}$$

Notably, the fitting coefficient for the porosity $1/M_0^* = 7.3$ is found to be in the range of values found experimentally by Knudsen (1959).

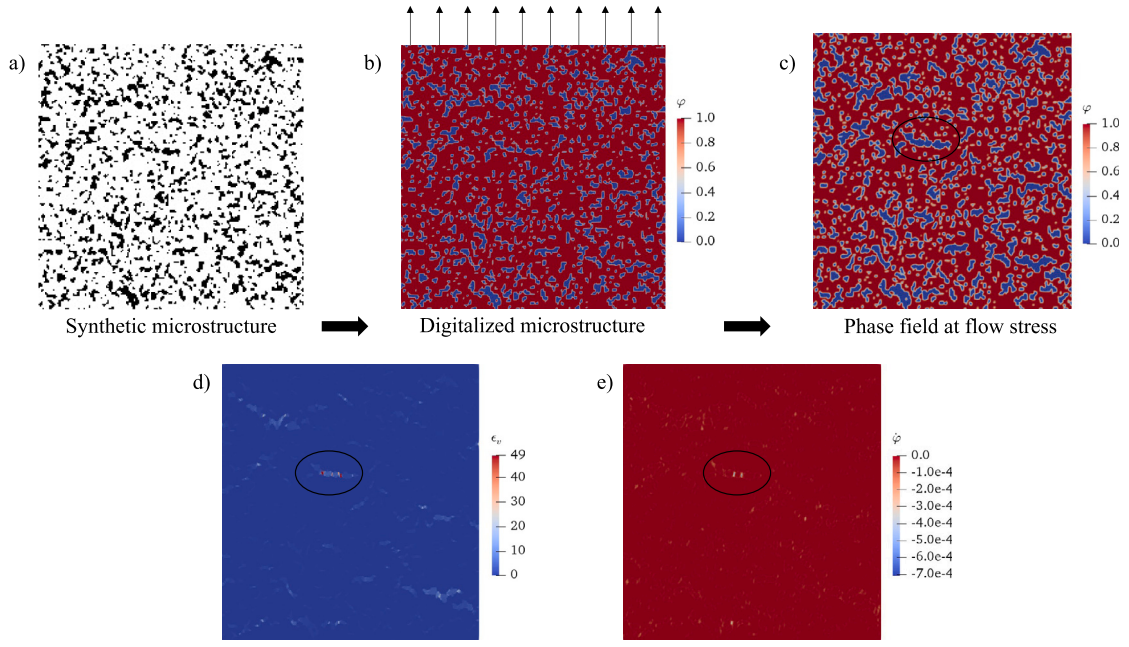

Fig. 7. a) SM generated for $n = 0.2$ and $h = 5$. b) Digitization of the SM used as input for φ. c) Output for φ after tensile loading post-yield for a vertical strain of $\epsilon_s = 11.5\%$. d) Volumetric strain distribution for the same state, concentrated in a central zone (black oval). e) Distribution of $\dot{\varphi}$ for the same state, negative since the pore phase $\varphi = 0$ is produced, with maximum absolute value also in the central zone, coinciding with the concentration of mechanical energy.

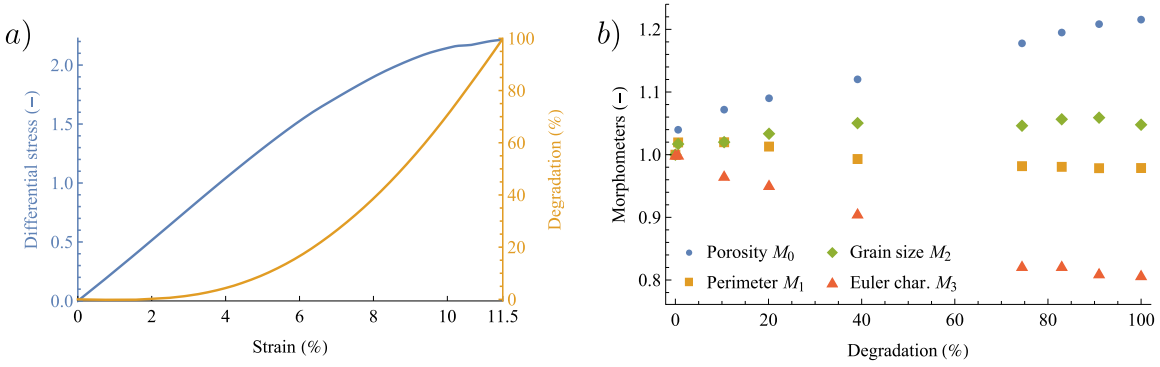

Fig. 8. a) Stress–strain curve (in blue) corresponding to the evolution of the SM presented in Fig. 7, along with the degradation–strain curve (in orange). b) Evolution of the morphometers with the degradation, whose values are normalized with their final values. Note that the values of the Euler characteristic M_3 is negative before normalization.

The prediction is found to be as accurate when replacing M_2 by M_3. We check that a Hall–Petch type of fitting with respect to the mean grain size M_2 is also satisfying, while keeping the exponential dependence for M_0 and M_1. We find that σ_s increases with the total perimeter M_1 and with the absolute value of the Euler characteristic M_3. We also check that it decreases with the porosity M_0 and with the grain size M_2, as already well known. For a given random seed, the prediction is thus found to be erroneous by less than 3% on average. Then, since choosing a seed amounts to an error of approximatively 4.33% (see Section 3.5), we infer that the overall predictive error is $\sqrt{2.67^2 + 4.33^2} \approx 5\%$. To use the latter formula, we have assumed that the error propagation is multiplicative, since the choice of the seed and of the morphometry is concomitant. This error estimation relies, however, on assuming that the stochastic error of 4.33% is valid for all the SMs, which is not here verified.

4.2. Comparison with experimental results

As previously discussed, experiments on a wide range of materials have shown that the strength depends exponentially on the porosity (see Ryshkewitch (1953), Knudsen (1959), Appendix A). Similarly, the relationship between strength and grain size is usually accurately described by a power law (Knudsen, 1959). We found above that this relationship is also adequately described by a exponential function. However, there are few results, if any, relating the strength to the two other morphometers, the surface area M_2 and the Euler number M_3, which could have corroborated our results. Furthermore, as emphasized in the present work, the strength should not depend, in general, on a single morphometer, but simultaneously on three of them in 2D (four in 3D). We use Knudsen's experimental data on ceramics (Knudsen, 1959), as regards the simultaneous dependence on porosity and grain size, to check the validity of Eq. (15) when the dependence on M_1

Table 3
Different fitting models with associated adjusted r^2 coefficient and average error, showing that the best fitting function is exponential, where $f_1(M_0, M_1, M_2) = \alpha_1 e^{\alpha_2 M_0 + \alpha_3 M_1 + \alpha_4 M_2}$, $f_2(M_0, M_1, M_3) = \alpha_1 e^{\alpha_2 M_0 + \alpha_3 M_1 + \alpha_4 M_3}$, $f_3(M_0, M_1, M_2) = \alpha_1 M_0^{\alpha_2} M_1^{\alpha_3} M_2^{\alpha_4}$, $f_4(M_0, M_1, M_2) = \alpha_1 e^{\alpha_2 M_0 + \alpha_3 M_1} M_2^{-0.5}$, $f_5(M_0, M_1, M_2) = \alpha_1 M_0 + \alpha_2 M_1 + \alpha_3 M_2$. The fitting coefficients α_i are determined via the least squares method.

Best fit	Exponential (M_0, M_1, M_2)	Exponential (M_0, M_1, M_3)	Power	Hall–Petch	Linear
Adjusted r^2	0.9995	0.9995	0.9963	0.9991	0.9739
Average error (%)	2.67	2.67	7.70	3.56	18.35
Fitting function	$f_1(M_0, M_1, M_2)$	$f_2(M_0, M_1, M_3)$	$f_3(M_0, M_1, M_2)$	$f_4(M_0, M_1, M_2)$	$f_5(M_0, M_1, M_2)$

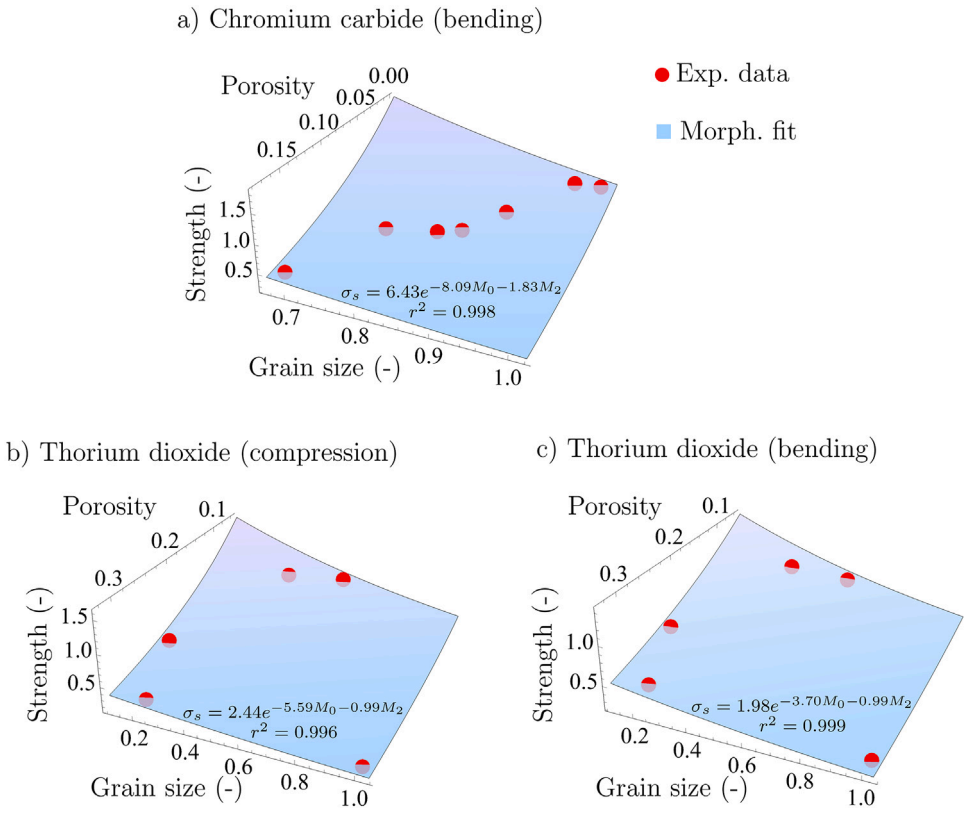

Fig. 9. Fitting of Knudsen's experimental data on ceramics (Knudsen, 1959) (red dots) with the morphometric strength law Eq. (15) (blue hyperplane) when the strength is approximated to depend only on the porosity M_0 and the grain size M_2. a) Strength of chromium carbide under bending (Table 8 in Knudsen (1959), temperature 1426 °C), fitted with an adjusted r^2 coefficient of 0.998. b) Strength of thorium dioxide under compression (Table 6 in Knudsen (1959)), fitted with an adjusted r^2 coefficient of 0.996. c) Strength of thorium dioxide under bending (Table 4 in Knudsen (1959)), fitted with an adjusted r^2 coefficient of 0.999. The values of strengths and grain sizes are normalized by their respective maximum values.

and M_3 is dropped (see Fig. 9). The adequacy of the fitting suggests that, at least for certain materials with relatively regular microstructure such as ceramics, not all morphometers are necessary. We will see in the following, however, that for more irregular microstructures like rocks or bones, this is not satisfactory in general. We also corroborate Knudsen's observation that the nature of the morphometric function in Eq. (15), namely exponential here, should be valid in compression, tension, or bending.

4.3. Dependence of the strength on the confinement

While the focus of this work concerns the morphometry, the strength can depend on other factors such as the confining pressure P, which we shall briefly discuss here. Such dependence can be included in the reference stress σ_s^*. We determine it by performing simulations of axisymmetric biaxial compressions for different values of P, for a given microstructure with values of porosity and heterogeneity in the middle range of our training batch ($n = 0.3$, $h = 3$), in plane strain conditions. To constrain the range of confining pressures, we estimate the preconsolidation pressure P_c by performing an isotropic compression (see Appendix E). By reading the yield stress value in Fig. E.17, we find an approximate value of $P_c \approx 1.2$. We then plot the obtained ϵ_s-strength with respect to the confining pressures (see Fig. 10), where the best fit function is a parabola. This recovers the parabolic failure criterion, recently suggested and experimentally verified (see Yuan et al., 2020; Wang et al., 2019; Singh and Rao, 2005). This also captures the transition from a linear behavior at low confining pressures to a pressure-insensitive behavior for high confinement (Yuan et al., 2020).

4.4. Strength prediction from real microstructures

To assess the validity of the morphometric strength law Eq. (15), "learned" on synthetic numerical data, we predict the strength of real

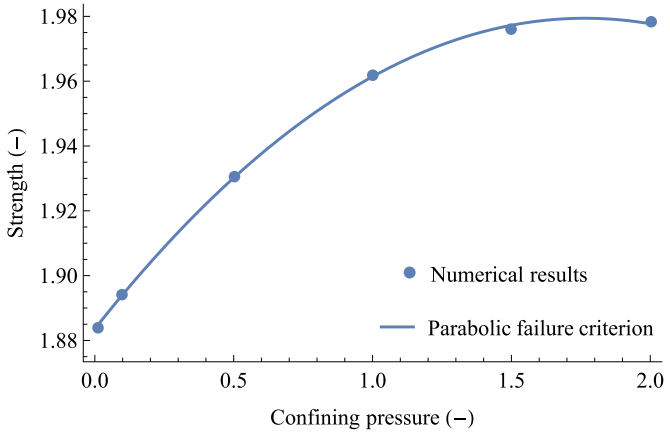

Fig. 10. The points represent numerical results for the strength versus the confining pressure in axisymmetric biaxial compression. The curve corresponds to the fit $-0.0308p^2 + 0.109p + 1.88$, for which the adjusted r^2 is exactly 1.

materials from CT scans, and compare it with phase-field simulations as previously. For that, we employ the following procedure. (1) We choose a set of m CT scans $C^1, \dots, C^m$ of a given material and pick one of them as the reference C^*. (2) We binarize the C^i and calculate the morphometers for each C^i as done previously for the SMs. In particular, this determines the reference values for the morphometers M_i^*. (3) We run one simulation for the reference CT scan C^* to determine the remaining reference value σ_s^*. (4) We deduce the σ_s^i for the remaining CT scans using the strength law. (5) We run the simulations for the remaining CT scans for comparison.

4.4.1. Geomaterials

Starting with geomaterials, we use CT scans[2] of Mt Simon and Berea sandstones, two benchmark rocks. The Mt Simon sandstone was introduced in Section 3.4. The Berea sandstone, of average porosity 17.9%, is presented in Lucas-Oliveira et al. (2020), with a digitization resolution of 2.25 µm per pixel. The resolution of the CT scans of both sandstones is reduced to 300 × 300 pixels to reduce the mesh size and have reasonable computation times, in particular yielding erroneously high porosity values in Table 4. This does not hinder the present qualitative study since the different parts of the Berea sandstone remain comparable with each others. Using the same model Eq. (13) and parameters values, we follow the procedure described above. The strength of the Mt Simon and Berea sandstones are defined with $\epsilon_s = 11.5\%$ and $\epsilon_s = 10\%$, respectively. The results are gathered in Fig. 13 and detailed in Fig. 11 and Table 4 for the example of a reference CT scan and a predicted strength for a weaker part with higher porosity. The predictions show a good agreement with an average error of 2.38% for the Mt Simon sandstone and 5.27% for the Berea sandstone. We must note that the choice of the reference CT scan C^* was made judiciously to minimize this error. For instance, for the Mt Simon sandstone, the average error for all choices of C^* was 3.53%. This pertains to the usual problem in modeling geomaterials, that is, finding a representative elementary domain. Indeed, it is sensible that in order to deduce the properties of a material's domain, one must use a representative domain as a reference. We also verify that predicting the strength with less morphometers than required by Hadwiger's theorem yields larger predictive errors. For example, for the Mt Simon sandstone, the prediction error increases by 43% when using the porosity M_0 and the grain size M_2 only.

[2] digitalrocksportal.org.

4.4.2. Bones

To showcase the general predictive power of the morphometric strength law Eq. (15), we perform the same predictive procedure for bones, which are porous materials exhibiting a wide range of porosities and microstructural architectures usually different from that of geomaterials. In particular, the example of bones enables us to address anisotropic microstructures. Since the Minkowski functionals are motion-invariant by definition, they cannot capture directionality; instead, one must use Minkowski tensors (Schröder-Turk et al., 2013) to have a morphometric description that depends on the direction. We leave this generalization for future works and concede that the following results on anisotropic microstructures are only valid for the loading direction considered here.

Typical values of morphometers for geomaterials and bones are shown in Table 4 for comparison. As far as the microstructure is concerned, there are two main kinds of bones, the cortical bone and the trabecular bone (see Cowin (2002) for a general review of bone mechanics). The former occupies the perimeter of the bone and has a low porosity ranging typically from 5 to 25%. The latter occupies the inside of the bone and has a scaffold microstructure, with a much higher porosity ranging from 50 to 90%. The main morphometer varying from a bone to another is the porosity. Indeed, the creation of porosity, because of age or disease, is the main sign of bone degradation. Thus, we will use our strength law to predict the strength of bones with varying porosities, given a reference bone, typically a healthy bone with a normal porosity.

For the trabecular bone, we used the CT scan in Fig. 1 of Neumann et al. (2018), providing a transverse section. We choose the healthy microstructure as the reference, to predict the strength of the arthritic one (see Fig. 12). As for the cortical bone, failing to find satisfying input images, we model it via SMs with anisotropy to resemble real cortical microstructures in their longitudinal section (see Fig. 9 in Cooper et al. (2004) and Fig. 1 in Granke et al. (2011)). For that, the heterogeneity h is chosen as an array $(1, 4)$, meaning that the pores are elongated in the vertical direction four times more than in the horizontal one (see Fig. 12). We then generate different SMs with varying porosities (3, 5, 7, 10, 15 and 20%) and fixed anisotropy.

We use the same model as previously, but with different elastic moduli for the skeleton phase. The same problem of determining the moduli of the skeleton phase holds as for geomaterials. Indeed, elastic moduli are usually measured for the mixture of the skeleton and pores phases. As explained in Section 2.3, we have assimilated the skeleton phase of geomaterials to a rock with very low porosity. Similarly, we assume the solid (mineral) phase of bones to be analogous to a bone of very low porosity, namely a cortical bone, for which the Lamé parameters can be found to be around 10 GPa and 7 GPa respectively (see Lai et al. (2015)). We define the ϵ_s-strength σ_s with $\epsilon_s = 15\%$ for the trabecular bone and $\epsilon_s = 25\%$ for the cortical bone. For the trabecular bone, since we use transverse sections, the loading is compressive. As for the cortical bone, modeled longitudinally, we choose a tensile loading. In agreement with (Morgan et al., 2018), we find that for a given post-yield vertical strain, the trabecular microstructure, in compression, has a softening response, whereas the cortical SM, in tension, is limited to a hardening response (see Fig. 12). For the synthetic cortical bones, we show for instance the results for $n = 15\%$ as a healthy bone and $n = 20\%$ as the arthritic bone to be predicted. Finally, we show a relatively accurate prediction of the strength from our morphometric law (see Fig. 13), with an error of 0.65% for the trabecular bone (detailed in Table 4), and an average error of 2.4% for the synthetic trabecular bones. For the latter, the accurate prediction required using two different reference microstructures, one for $n < 10\%$ and one for $n \geq 10\%$, indicating that the material may have two distinct mechanical behaviors for those two ranges of porosities. We have used the Euler characteristic M_3 instead of the grain size M_2 since determining the grain size distributions is, as expected, less accurate for microstructures with little convexity and may not bear any physical meaning. As for

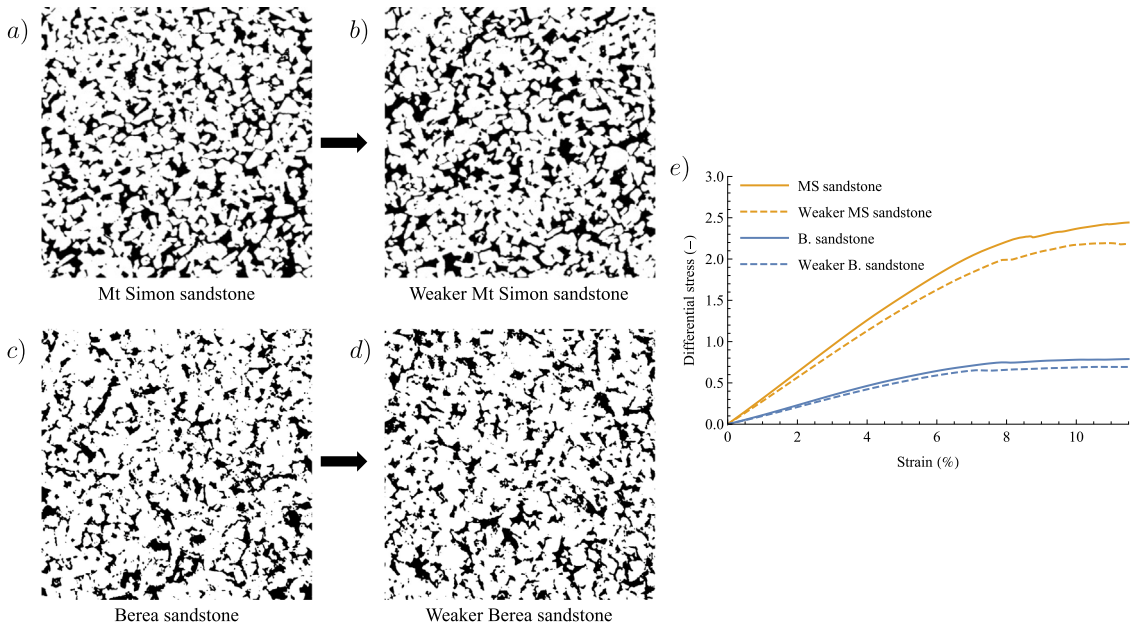

Fig. 11. a) CT scans of a Mt Simon sandstone (layer 108) and b) another layer of the same sandstone (890) with 8% increase of porosity with similar other morphometers, hence weaker. c) CT scans of a Berea sandstone (layer 000) and d) another layer of the same sandstone (940) with 7% increase of porosity with similar other morphometers, hence weaker. e) Mechanical response of the 4 sandstones microstructures.

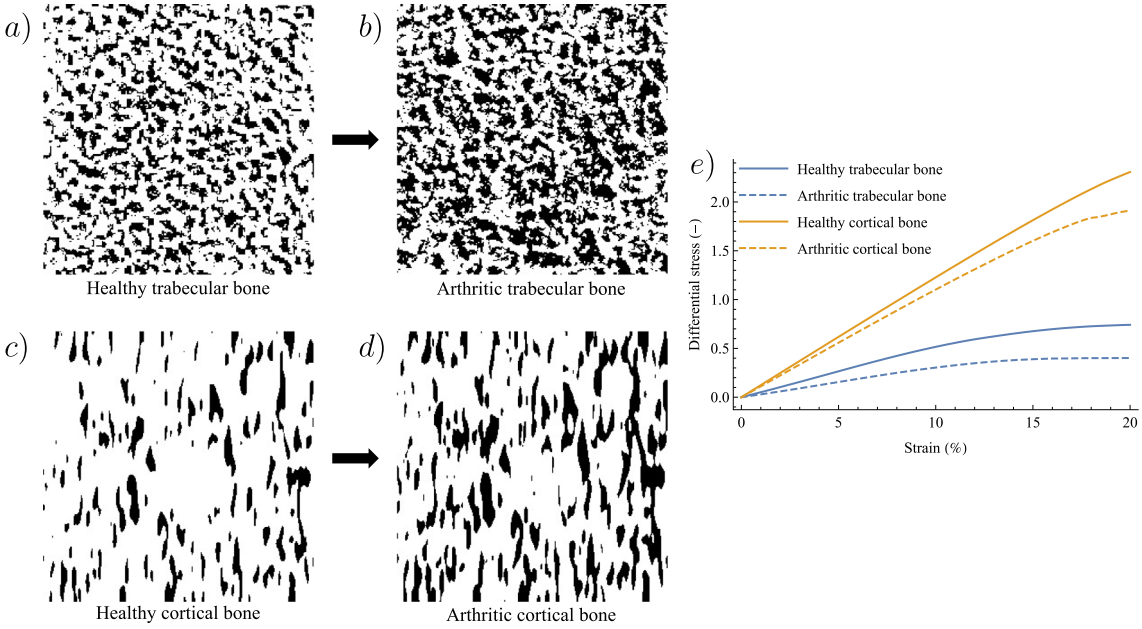

Fig. 12. a) CT scans of a healthy and b) arthritic trabecular bone's microstructure (from Neumann et al., 2018). c) Synthetic microstructures of a healthy (15% porosity) and d) arthritic (20% porosity) cortical bone. e) Mechanical response of the 4 bones.

the geomaterials, we also calculate the prediction error made in using only two morphometers, here the porosity M_0 and the perimeter M_1. In the case of the trabecular bone, the error soars from 0.65% to 46.2%. Such an increase is expected insofar as the trabecular bone has the most irregular microstructure studied in this work, and therefore, demands the most information to be described. In all, the average errors between predicted and simulated strengths are of the same order as the expected maximum prediction error calculated in Section 4.1.

5. Conclusion

We have suggested from qualitative 2D numerical simulations on synthetic and real microstructures the possibility to fully account for the morphometry of porous media in their macroscopic properties, such as the strength. To do so, we have used a damage phase-field modeling of the microstructure, capturing the exact microstructural geometry and encapsulating causes of damage such as debonding, dissolution and microcracks. The necessary and sufficient microstructural information is then upscaled in the form of morphometers defined from Minkowski functionals, as per Hadwiger's theorem. In the context of porous media, the four morphometers are chosen as the porosity, the total surface area of the skeleton, the mean grain size and the Euler characteristic; only three of them are required in 2D. We have inferred from a wide range of synthetic microstructures, with various porosities and heterogeneities, that the strength is best described by an exponential function of the morphometers. Those generated microstructures were

Table 4
Details of the prediction of the strength of the Mt Simon and Berea sandstones and of the trabecular and cortical bones, for one reference and one prediction.

	M_0 (%)	M_1 (mm)	M_2 (μm)	M_3	σ_s (numerics)	σ_s (predicted)	Error (%)
Mt Simon sandstone	20.6	142	118	/	2.44	[a]	/
Weaker MS sandstone	22.2	145	121	/	2.18	2.24	2.72
Berea sandstone	37.7[b]	253	7.96	/	0.780	[a]	/
Weaker B. sandstone	40.2[b]	253	8.35	/	0.687	0.697	1.41
Healthy trabecular bone	29.5	451	/	−423	0.676	[a]	/
Arthritic trabecular bone	41.1	552	/	−265	0.389	0.391	0.645
Healthy cortical bone	15	101	/	−97	2.51	[a]	/
Arthritic cortical bone	20	125	/	−91	1.97	2.02	2.60

[a]Reference CT scans.
[b]Porosities larger than real values from lowering initial resolution.

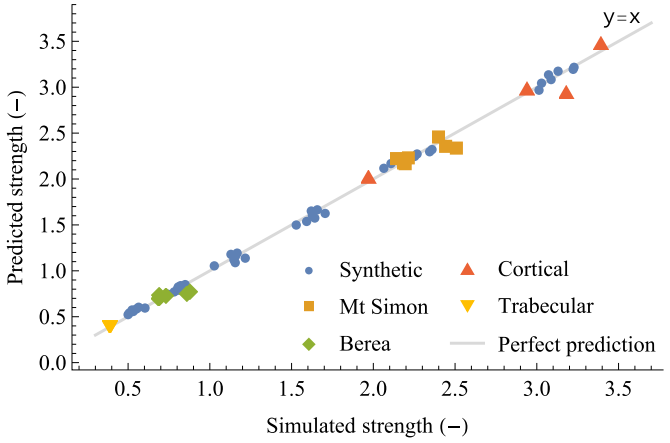

Fig. 13. Predicted strength with the morphometric strength law Eq. (15) versus the strength obtained from phase-field simulations, for SMs, geomaterials (Mt Simon and Berea sandstones) and biomaterials (trabecular bones and synthetic cortical bones).

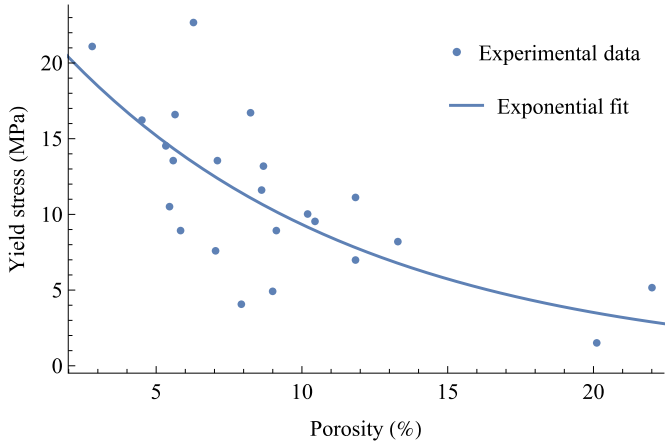

Fig. A.14. Exponential fit of the yield stress evolution with porosity for cortical bones. *Source:* Adapted from the experimental results of Wachter et al. (2002).

checked to resemble real microstructures via the lognormal distribution of their morphometers. When compared with phase-field simulations, the exponential strength law was also verified to be accurate for two subclasses of porous media, geomaterials (sandstones) and biomaterials (bones), from digitalized CT scans. We also find that this law, as a function of porosity and grain size only, accurately matches experimental data for different ceramics. The strength prediction only requires the initial values of the morphometers for a given material's sample, along with the reference strength and morphometers values from another microstructure made of the same material.

The overarching goal is to predict the behavior of porous media with the minimal amount of data possible and in particular, minimizing the use of destructive tests in favor of remote sensing. This is of interest in geosciences where samples may be inaccessible and in biosciences where materials are best studied in vivo. The following steps in this endeavor will include 3D modeling and most importantly, experimental corroboration of the morphometric strength law. Indeed, experimental data are missing for the simultaneous dependence of strength on multiple morphometers, in particular including the surface area and the Euler characteristic. Then, the influence of environmental factors, like temperature and acidity, may be incorporated in a similar fashion. Building on aforementioned works, machine learning may also be used to ensure the realism of the synthetic microstructures. Classical constitutive laws, such as viscoplasticity, may be re-explored to explicitly include the morphometric dependence. Apart from mechanical characterization, other components of the multiphysics of porous media can be investigated through their morphometry, such as fluid flow (Armstrong et al., 2016, 2019). A major impediment to such program, albeit common to any modeling of heterogeneous microstructures, is that the reference sample must be representative of the material. This holistic description opens new avenues for modeling porous media in general, including geomaterials, biomaterials and engineered materials, at least as far as the microstructural geometry is concerned. It is indeed of paramount interest to draw bridges between the progress in different disciplines concerned with the same problematics.

Declaration of competing interest

The authors declare that they have no known competing financial interests or personal relationships that could have appeared to influence the work reported in this paper.

Acknowledgments

The authors Alexandre Guével and Manolis Veveakis gratefully acknowledge the support of the U.S. Department of Energy grant DE-NE0008746 and the U.S. National Science Foundation for project CMMI-2042325.

Appendix A. Exponential relationship between strength and porosity for bones

See Fig. A.14.

Appendix B. Summary table

See Fig. B.15.

h	M_0	M_1 (px)	M_2 (px)	M_3	σ_s (numerical)	σ_s (predicted)	Error (%)
2	0.15	3054	12.84	-117	3.01	2.97	1.49
2.5	0.15	3532	11.07	-167	3.03	3.04	0.44
3	0.15	3941	10.54	-252	3.09	3.08	0.17
3.5	0.15	4287	9.45	-356	3.07	3.13	1.99
4	0.15	4759	9.10	-473	3.13	3.17	1.39
4.5	0.15	4808	8.49	-599	3.22	3.19	0.93
5	0.15	4961	8.06	-742	3.23	3.21	0.42
2	0.2	3796	11.51	-98	2.06	2.12	2.55
2.5	0.2	4376	10.12	-168	2.11	2.17	2.83
3	0.2	4985	9.51	-255	2.15	2.21	2.46
3.5	0.2	5515	8.69	-352	2.25	2.25	0.26
4	0.2	5915	8.26	-478	2.27	2.27	0.27
4.5	0.2	6203	7.71	-600	2.34	2.30	1.98
5	0.2	6461	7.14	-735	2.36	2.32	1.59
2	0.25	4361	10.62	-86	1.53	1.50	1.96
2.5	0.25	5154	9.50	-153	1.59	1.54	3.40
3	0.25	5934	8.55	-236	1.64	1.58	4.03
3.5	0.25	6550	8.04	-321	1.63	1.60	1.46
4	0.25	7056	7.53	-427	1.71	1.63	4.56
4.5	0.25	7487	6.71	-546	1.62	1.65	2.04
5	0.25	7798	6.50	-659	1.66	1.67	0.60
2	0.3	4816	10.23	-74	1.03	1.05	2.59
2.5	0.3	5844	8.86	-132	1.16	1.09	5.71
3	0.3	6724	8.05	-197	1.15	1.12	2.27
3.5	0.3	7483	7.57	-264	1.22	1.14	6.30
4	0.3	8119	6.67	-345	1.16	1.16	0.55
4.5	0.3	8672	6.21	-449	1.13	1.18	4.71
5	0.3	9076	5.82	-568	1.17	1.20	2.50
2	0.35	5241	9.20	-50	0.74	0.74	0.06
2.5	0.35	6436	8.09	-98	0.78	0.77	1.42
3	0.35	7389	7.51	-149	0.81	0.79	2.32
3.5	0.35	8283	6.78	-202	0.80	0.81	0.82
4	0.35	9010	6.21	-284	0.81	0.83	2.47
4.5	0.35	9639	5.77	-359	0.82	0.84	2.42
5	0.35	10136	5.33	-487	0.85	0.85	0.45
2	0.4	5541	8.59	-35	0.50	0.52	4.50
2.5	0.4	6895	7.44	-55	0.51	0.54	6.61
3	0.4	7942	6.94	-96	0.53	0.56	4.97
3.5	0.4	8944	5.93	-150	0.52	0.57	9.58
4	0.4	9816	5.67	-185	0.55	0.59	6.42
4.5	0.4	10459	5.32	-257	0.55	0.60	1.12
5	0.4	11043	4.89	-342	0.56	0.61	7.38

Fig. B.15. Summary table gathering the morphometers of the SMs, with corresponding strengths obtained numerically with phase-field simulations, versus the strengths predicted with the morphometric strength law, along with the associated prediction error. The predicted strength is found to be best predicted with the exponential function $\sigma_s = 9.2251e^{-7.2947n+0.8511p-1.6305g}$, obtained from `Mathematica`'s function `NonlinearModelFit`.

Appendix C. Calculations of the morphometers

The morphometers are calculated via the Python libraries `PoreSpy` et `skimage`, as described in the following table. The segmentation of the SMs is performed via the SNOW algorithm introduced in Gostick (2017), using the function `filters.snow_partitioning` in `PoreSpy` (see Table C.5).

Table C.5
* The function `pore.diameter` was initially defined (and named) to calculate the sizes of the pores obtained from segmentation. However, it can be applied to calculate the grain size when applied on the segmentation of the grains.

Morphometer	Library	Function
Porosity M_0	`PoreSpy`	`metrics.porosity`
Perimeter M_1	`skimage`	`measure.perimeter`
Grain size M_2	`PoreSpy`	`pore.diameter*`
Euler number M_3	`skimage`	`measure.euler_number`

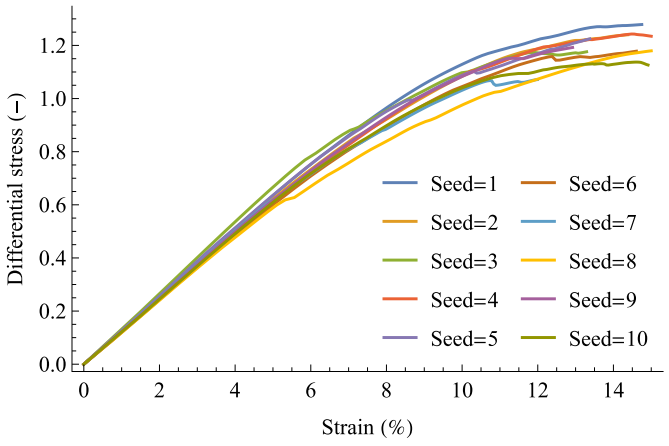

Fig. D.16. Mechanical response for different random seeds for the SM $n = 0.3$, $h = 3$.

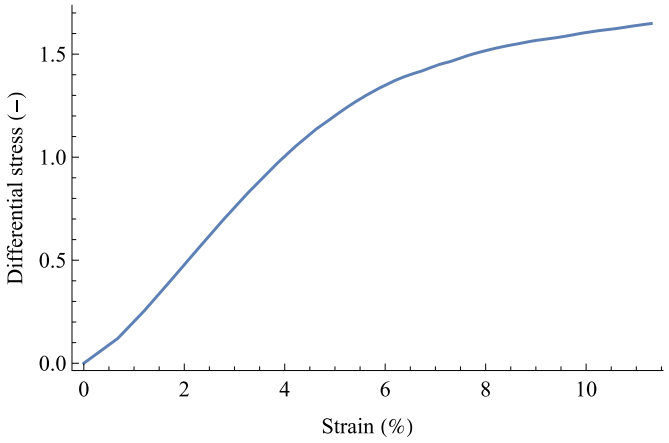

Fig. E.17. Stress–strain curve of the isotropic compression simulation determining the preconsolidation stress, taken as the yield stress of this curve and found to be around 1.2.

Appendix D. Determinism of the SMs

See Fig. D.16.

Appendix E. Preconsolidation

See Fig. E.17.

References

Aagesen, L.K., Schwen, D., Ahmed, K., Tonks, M.R., 2017. Quantifying elastic energy effects on interfacial energy in the Kim-Kim-Suzuki phase-field model with different interpolation schemes. Comput. Mater. Sci. 140, 10–21. http://dx.doi.org/10.1016/j.commatsci.2017.08.005.

Allen, S.M., Cahn, J.W., 1979. A microscopic theory for antiphase boundary motion and its application to antiphase domain coarsening. Acta Metall. 27, 1085–1095. http://dx.doi.org/10.1016/0001-6160(79)90196-2.

Ammar, K., Appolaire, B., Cailletaud, G., Forest, S., 2009. Combining phase field approach and homogenization methods for modelling phase transformation in elastoplastic media. Rev. Eur. Méc. Numér. 18, 485–523. http://dx.doi.org/10.3166/ejcm.18.485-523.

Armstrong, R.T., McClure, J.E., Berrill, M.A., Rücker, M., Schlüter, S., Berg, S., 2016. Beyond Darcy's law: The role of phase topology and ganglion dynamics for two-fluid flow. Phys. Rev. E 94, http://dx.doi.org/10.1103/PhysRevE.94.043113.

Armstrong, R.T., McClure, J.E., Robins, V., Liu, Z., Arns, C.H., Schlüter, S., Berg, S., 2019. Porous media characterization using Minkowski functionals: Theories, applications and future directions. Transp. Porous Media 130, 305–335. http://dx.doi.org/10.1007/s11242-018-1201-4.

Augat, P., Schorlemmer, S., 2006. The role of cortical bone and its microstructure in bone strength. Age Ageing 35, 27–31. http://dx.doi.org/10.1093/ageing/afl081.

Benkrid, K., Crookes, D., Benkrid, A., 2000. Design and fpga implementation of a perimeter estimator. In: Proceedings of the Irish Machine Vision and Image Processing Conference. pp. 51–57.

Bhattacharyya, S., Sahara, R., Ohno, K., 2019. A first-principles phase field method for quantitatively predicting multi-composition phase separation without thermodynamic empirical parameter. Nature Commun. 10, 1–2. http://dx.doi.org/10.1038/s41467-019-11248-z.

Biot, M.A., 1941. General theory of three-dimensional consolidation. J. Appl. Phys. 12, 155–164.

Buscarnera, G., Einav, I., 2021. The mechanics of brittle granular materials with coevolving grain size and shape. Proc. R. Soc. A 477, doi:20201005.

Chun, S., Roy, S., Nguyen, Y.T., Choi, J.B., Udaykumar, H.S., Baek, S.S., 2020. Deep learning for synthetic microstructure generation in a materials-by-design framework for heterogeneous energetic materials. Sci. Rep. 10, 1–15. http://dx.doi.org/10.1038/s41598-020-70149-0.

Cooper, D.M., Matyas, J.R., Katzenberg, M.A., Hallgrimsson, B., 2004. Comparison of microcomputed tomographic and microradiographic measurements of cortical bone porosity. Calcif. Tissue Int. 74, 437–447. http://dx.doi.org/10.1007/s00223-003-0071-z.

Coussy, O., 2004. Poromechanics. Wiley, http://dx.doi.org/10.1002/0470092718.

Cowin, S.C. (Ed.), 2002. Bone Mechanics Handbook. CRC Press, http://dx.doi.org/10.1115/1.1579463.

Croizé, D., Renard, F., Gratier, J.P., 2013. Compaction and porosity reduction in carbonates: A review of observations, theory, and experiments. In: Advances in Geophysics, Vol. 54. Elsevier Inc., pp. 181–238. http://dx.doi.org/10.1016/B978-0-12-380940-7.00003-2.

Dormieux, L., Kondo, D., Ulm, F.J., 2006. Microporomechanics. John Wiley and Sons Inc.

Einav, I., 2007. Breakage mechanics-Part I: Theory. J. Mech. Phys. Solids 55, 1274–1297. http://dx.doi.org/10.1016/j.jmps.2006.11.003.

van den Ende, M.P., Niemeijer, A.R., Spiers, C.J., 2019. Influence of grain boundary structural evolution on pressure solution creep rates. J. Geophys. Res.: Solid Earth 1–30. http://dx.doi.org/10.1029/2019JB017500.

Fischer, G.J., Paterson, M.S., 1989. Dilatancy during rock deformation at high temperatures and pressures. J. Geophys. Res.: Solid Earth 94, 17607–17617. http://dx.doi.org/10.1029/JB094iB12p17607, https://agupubs.onlinelibrary.wiley.com/doi/abs/10.1029/JB094iB12p17607.

Fragogeorgi, E.A., Rouchota, M., Georgiou, M., Velez, M., Bouziotis, P., Loudos, G., 2019. In vivo imaging techniques for bone tissue engineering. J. Tissue Eng. 10, http://dx.doi.org/10.1177/2041731419854586.

Fried, E., Gurtin, M.E., 1993. Continuum theory of thermally induced phase transitions based on an order parameter. Physica D 68, 326–343. http://dx.doi.org/10.1016/0167-2789(93)90128-N.

Gonzalez, R.C., Woods, R.E., 2008. Digital Image Processing. Prentice Hall.

Gostick, J.T., 2017. Versatile and efficient pore network extraction method using marker-based watershed segmentation. Phys. Rev. E 96, 1–15. http://dx.doi.org/10.1103/PhysRevE.96.023307.

Gostick, J., Khan, Z., Tranter, T., Kok, M., Agnaou, M., Sadeghi, M., Jervis, R., 2019. PoreSpy: A python toolkit for quantitative analysis of porous media images. J. Open Source Softw. 4, 1296. http://dx.doi.org/10.21105/joss.01296.

Granke, M., Grimal, Q., Saïed, A., Nauleau, P., Peyrin, F., Laugier, P., 2011. Change in porosity is the major determinant of the variation of cortical bone elasticity at the millimeter scale in aged women. Bone 49, 1020–1026. http://dx.doi.org/10.1016/j.bone.2011.08.002.

Guével, A., Rattez, H., Veveakis, E., 2020. Viscous phase-field modeling for chemo-mechanical microstructural evolution: application to geomaterials and pressure solution. Int. J. Solids Struct. 207, 230–249. http://dx.doi.org/10.1016/j.ijsolstr.2020.09.026.

Gurtin, M.E., 1996. Generalized Ginzburg–Landau and Cahn-Hilliard equations based on a microforce balance. Physica D 92, 178–192. http://dx.doi.org/10.1155/S1110757X03204083.

Hadwiger, H., 1951. The deformation and ageing of mild steel: III Discussion of results. Proc. Phys. Soc. B 64, 747–753.

Hall, E.O., 1951. The deformation and ageing of mild steel: III Discussion of results. Proc. Phys. Soc. B 64, 747–753. http://dx.doi.org/10.1088/0370-1301/64/9/303.

Huyghe, J.M., Loon, R.V., Kemenade, P.M.V., Smit, T.H., Perfusion, B., 2002. We all are porous media. In: Poromechanics II. pp. 17–28.

Hwang, S.I., Powers, S.E., 2003. Lognormal distribution model for estimating soil water retention curves for sandy soils. Soil Sci. 168, 156–166. http://dx.doi.org/10.1097/01.ss.0000058888.60072.e3.

Kawamoto, R., Andò, E., Viggiani, G., Andrade, J.E., 2018. All you need is shape: Predicting shear banding in sand with LS-DEM. J. Mech. Phys. Solids 111, 375–392. http://dx.doi.org/10.1016/j.jmps.2017.10.003.

Klain, D.A., 1995. A short proof of Hadwiger's characterization theorem. Mathematika 42, 329–339. http://dx.doi.org/10.1112/S0025579300014625.

Knudsen, F.P., 1959. Dependence of mechanical strength of brittle polycrystalline specimens on porosity and grain size. J. Am. Ceram. Soc. 42, 376–387. http://dx.doi.org/10.1111/j.1151-2916.1959.tb13596.x.

Kohanpur, A.H., Rahromostaqim, M., Valocchi, A.J., Sahimi, M., 2020. Two-phase flow of CO2-brine in a heterogeneous sandstone: Characterization of the rock and comparison of the lattice-Boltzmann, pore-network, and direct numerical simulation methods. Adv. Water Resour. 135, http://dx.doi.org/10.1016/j.advwatres.2019.103469.

Kuhn, C., Müller, R., 2010. A continuum phase field model for fracture. Eng. Fract. Mech. 77, 3625–3634. http://dx.doi.org/10.1016/j.engfracmech.2010.08.009.

Lai, Y.S., Chen, W.C., Huang, C.H., Cheng, C.K., Chan, K.K., Chang, T.K., 2015. The effect of graft strength on knee laxity and graft in-situ forces after posterior cruciate ligament reconstruction. PLoS ONE 10, http://dx.doi.org/10.1371/journal.pone.0127293.

Landau, L.D., 1937. On the theory of phase transitions. Zh. Eks. Teor. Fiz. 7, 19–32. http://dx.doi.org/10.1038/138840a0.

Lesueur, M., Poulet, T., Veveakis, M., 2020. Three-scale multiphysics finite element framework (FE3) modelling fault reactivation. Comput. Methods Appl. Mech. Engrg. 365, http://dx.doi.org/10.1016/j.cma.2020.112988.

Li, Y., Bushby, A.J., Dunstan, D.J., 2016. The hall-petch effect as a manifestation of the general size effect. Proc. R. Soc. A 472, http://dx.doi.org/10.1098/rspa.2015.0890.

Liu, D., Šavija, B., Smith, G.E., Flewitt, P.E., Lowe, T., Schlangen, E., 2017. Towards understanding the influence of porosity on mechanical and fracture behaviour of quasi-brittle materials: experiments and modelling. Int. J. Fract. 205, 57–72. http://dx.doi.org/10.1007/s10704-017-0181-7.

Lucas-Oliveira, E., Araujo-Ferreira, A.G., Trevizan, W.A., Coutinho dos Santos, B.C., Bonagamba, T.J., 2020. Sandstone surface relaxivity determined by NMR T2 distribution and digital rock simulation for permeability evaluation. J. Pet. Sci. Eng. 193, 107400. http://dx.doi.org/10.1016/j.petrol.2020.107400.

Marks, B., Einav, I., 2015. A mixture of crushing and segregation: The complexity of grainsize in natural granular flows. Geophys. Res. Lett. 42, 274–281. http://dx.doi.org/10.1002/2014GL062470.

Mecke, K., Arns, C.H., 2005. Fluids in porous media: A morphometric approach. J. Phys. Condens. Matter 17, http://dx.doi.org/10.1088/0953-8984/17/9/014.

Morgan, E.F., Unnikrisnan, G.U., Hussein, A.I., 2018. Bone mechanical properties in healthy and diseased states. Annu. Rev. Biomed. Eng. 20, 119–143. http://dx.doi.org/10.1146/annurev-bioeng-062117-121139.

Mosser, L., Dubrule, O., Blunt, M.J., 2017. Reconstruction of three-dimensional porous media using generative adversarial neural networks. Phys. Rev. E 96, http://dx.doi.org/10.1103/PhysRevE.96.043309.

Neumann, A., Haschka, J., Kleyer, A., Schuster, L., Englbrecht, M., Berlin, A., Figueiredo, C.P., Simon, D., Muschitz, C., Kocijan, R., Resch, H., Rech, J., Schett, G., 2018. Cortical bone loss is an early feature of nonradiographic axial spondyloarthritis. Arthritis Res. Ther. 20, 1–11. http://dx.doi.org/10.1186/s13075-018-1620-1.

Niemeijer, A., Elsworth, D., Marone, C., 2009. Significant effect of grain size distribution on compaction rates in granular aggregates. Earth Planet. Sci. Lett. 284, 386–391. http://dx.doi.org/10.1016/j.epsl.2009.04.041.

Orowan, E., 1949. Fracture and strength of solids. Rep. Progr. Phys. 12, 185–232.

O'Sullivan, C., 2011. Particulate Discrete Element Modelling: A Geomechanics Perspective. Spon Press.

Pardoen, T., Hutchinson, J.W., 2000. Extended model for void growth and coalescence. J. Mech. Phys. Solids 48, 2467–2512. http://dx.doi.org/10.1016/S0022-5096(00)00019-3.

Permann, C.J., Gaston, D.R., Andrš, D., Carlsen, R.W., Kong, F., Lindsay, A.D., Miller, J.M., Peterson, J.W., Slaughter, A.E., Stogner, R.H., Martineau, R.C., 2020. MOOSE: Enabling massively parallel multiphysics simulation. SoftwareX 11, 100430. http://dx.doi.org/10.1016/j.softx.2020.100430.

Petch, N.J., 1953. The cleavage strength of polycrystals. J. Iron Steel Inst. 174, 25–28.

Provatas, N., Elder, K., 2010. Phase-Field Methods in Material Science and Engineering. Wiley-VCH, p. 312. http://dx.doi.org/10.1002/9783527631520.

Rattez, H., Stefanou, I., Sulem, J., 2018a. The importance of Thermo-Hydro-Mechanical couplings and microstructure to strain localization in 3D continua with application to seismic faults. Part I: Theory and linear stability analysis. J. Mech. Phys. Solids 115, 54–76. http://dx.doi.org/10.1016/j.jmps.2018.03.004.

Rattez, H., Stefanou, I., Sulem, J., Veveakis, M., Poulet, T., 2018b. The importance of Thermo-Hydro-Mechanical couplings and microstructure to strain localization in 3D continua with application to seismic faults. Part II: Numerical implementation and post-bifurcation analysis. J. Mech. Phys. Solids 115, 1–29. http://dx.doi.org/10.1016/j.jmps.2018.03.003.

Ryshkewitch, E., 1953. Compression strength of porous sintered alumina and zirconia. J. Am. Ceram. Soc. 36, 65–68. http://dx.doi.org/10.1016/b978-0-408-15960-9.50076-0.

Salvini, V.R., Pandolfelli, V.C., Spinelli, D., 2018. Mechanical properties of porous ceramics. In: Recent Advances in Porous Ceramics. http://dx.doi.org/10.5772/intechopen.71612.

Sari, M., Alevizos, S., Poulet, T., Lin, J., Veveakis, M., 2020. A visco-plastic framework for interface processes in sedimentary reservoir rocks at HPHT conditions. Geomech Energy Environ 22, 100165. http://dx.doi.org/10.1016/j.gete.2019.100165.

Schröder-Turk, G.E., Mickel, W., Kapfer, S.C., Schaller, F.M., Breidenbach, B., Hug, D., Mecke, K., 2013. Minkowski tensors of anisotropic spatial structure. New J. Phys. 15, http://dx.doi.org/10.1088/1367-2630/15/8/083028.

Singh, M., Rao, K.S., 2005. Bearing capacity of shallow foundations in anisotropic Non-Hoek–Brown rock masses. J. Geotech. Geoenviron. Eng. 131, 1014–1023. http://dx.doi.org/10.1061/(asce)1090-0241(2005)131:8(1014).

Terzaghi, K., 1943. Theoretical Soil Mechanics. John Wiley and Sons Inc, http://dx.doi.org/10.1680/geot.1964.14.1.1.

Tonks, M., Millett, P., 2011. Phase field simulations of elastic deformation-driven grain growth in 2D copper polycrystals. Mater. Sci. Eng. A 528, 4086–4091. http://dx.doi.org/10.1016/j.msea.2011.02.007.

Tourret, D., Liu, H., LLorca, J., 2021. Phase-field modeling of microstructure evolution: Recent applications, perspectives and challenges. Prog. Mater. Sci. 100810. http://dx.doi.org/10.1016/j.pmatsci.2021.100810.

Vardoulakis, I., Sulem, J., 1995. Bifurcation Analysis in Geomechanics. http://dx.doi.org/10.1201/9781482269383.

Veveakis, E., Poulet, T., Alevizos, S., 2014. Thermo-poro-mechanics of chemically active creeping faults. 1: Theory and steady state considerations. J. Geophys. Res.: Solid Earth 119, 4583–4605. http://dx.doi.org/10.1002/2013JB010071.

Vogel, H.J., 2002. Topological Characterization of Porous Media. Springer Berlin Heidelberg, Berlin, Heidelberg, pp. 75–92. http://dx.doi.org/10.1007/3-540-45782-8_3.

Wachter, N.J., Krischak, G.D., Mentzel, M., Sarkar, M.R., Ebinger, T., Kinzl, L., Claes, L., Augat, P., 2002. Correlation of bone mineral density with strength and microstructural parameters of cortical bone in vitro. Bone 31, 90–95. http://dx.doi.org/10.1016/S8756-3282(02)00779-2.

Wang, D.J., Tang, H., Shen, P., Cai, Y., 2019. A parabolic failure criterion for transversely isotropic rock: Modification and verification. Math. Probl. Eng. 2019, http://dx.doi.org/10.1155/2019/8052560.

Wetzel, M., Kempka, T., Kühn, M., 2021. Diagenetic trends of synthetic reservoir sandstone properties assessed by digital rock physics. Minerals 11, 1–21. http://dx.doi.org/10.3390/min11020151.

Yuan, C., Guo, Y., Wang, W., Cao, L., Fan, L., Huang, C., 2020. Study on triaxial loading-unloading-uniaxial loading and microscopic damage test of sandstone. Front. Earth Sci. 8, 1–11. http://dx.doi.org/10.3389/feart.2020.00078.

Zhang, Y.D., Buscarnera, G., Einav, I., 2016. Grain size dependence of yielding in granular soils interpreted using fracture mechanics, breakage mechanics and Weibull statistics. Geotechnique 66, 149–160. http://dx.doi.org/10.1680/jgeot.15.P.119.